Entropy-Mediated Polymer–Cluster Interactions Enable Dramatic Thermal Stiffening Hydrogels for Mechanoadaptive Smart Fabrics

Jia Wu, Baohu Wu, Jiaqing Xiong, Shengtong Sun, and Peiyi Wu**

Abstract: Thermal stiffening materials that are naturally soft but adaptively self-strengthen upon heat are intriguing for load-bearing and self-protection applications at elevated temperatures. However, to simultaneously achieve high modulus change amplitude and high mechanical strength at the stiffened state remains challenging. Herein, entropy-mediated polymer–mineral cluster interactions are exploited to afford thermal stiffening hydrogels with a record-high storage modulus enhancement of 13000 times covering a super wide regime from 1.3 kPa to 17 MPa. Such a dramatic thermal stiffening effect is ascribed to the transition from liquid-liquid to solid–liquid phase separations, and at the molecular level, driven by enhanced polymer–cluster interactions. The hydrogel is further processed into sheath–core fibers and smart fabrics, which demonstrate self-strengthening and self-powered sensing properties by co-weaving another liquid metal fiber as both the joule heater and triboelectric layer.

Introduction

In nature, it is a popular strategy for living matter to tune their mechanical properties to execute various intellectual functions, e.g. the sea cucumber rapidly hardens its skin as a means of protection, and muscles reversibly stiffen and soften for locomotion and object manipulation.[1] Inspired by the mechanical adaption of tissue, a number of artificial materials with the ability to alter their mechanical properties have been synthesized via the mechanisms of stimuli-induced phase separation,[2,3] filler aggregation,[4] jamming,[5] and self-polymerization.[6,7] Among them, thermal sensitive materials are of particular interest owing to their easy operation in either direct heating or indirect electro-/photo-/magneto-thermal ways. By delicately controlling the stiffness at different temperatures, thermal sensitive materials have gained wide applications in soft actuation, shape memory, self-healing, and tissue implantation.[8–11] Nevertheless, due to the abundance of enthalpy-dominated interactions involving dipolar, hydrogen bonding, and host–guest interactions, heat usually leads to the degradation of material's mechanical strength, which greatly hinders their load-bearing and self-protection applications at elevated temperatures.

To overcome the typical thermal softening effect of common materials, plenty of recent efforts have been devoted to developing thermal stiffening materials that can instantly self-strengthen upon heat with drastic modulus increase. The mostly adopted strategy is based on phase-transition hydrogels by incorporating LCST (lower critical solution temperature)-type polymers such as poly(*N*-isopropylacrylamide).[12–14] To inhibit the unwanted macroscopic volume contraction of LCST-type polymers, hydrophilic blocks are often introduced as molecular scaffolds to retain the released water at the micro- and meso-scales.[15–18] However, such a design usually leads to reduced modulus change amplitudes (generally <20 times) and the maximum moduli at the stiffened state are also low (<1 MPa). Grafting LCST-type polymers on nanoparticles to thermally induce percolating reinforcing network or particle jamming may greatly enhance material's mechanical strength at the stiffened state, yet the complicated manufacturing and elaborate control over particle assemblies largely limit their extensive applications.[4,19] As an alternative, Gong et al. recently reported a simply prepared, thermal stiffening, and isochoric poly(acrylic acid) (PAA)/calcium acetate hydrogel which showed 1800 times Young's modulus enhancement ($\approx$350 times storage modulus change) as well as high storage modulus at the stiffened state ($\approx$35 MPa).[20] The thermal stiffening effect is believed to arise from the reduced permittivity of calcium acetate and enhanced interchain interactions at high temperatures, and has enabled a few fascinating applications like thermoactivated protection,[20] switchable lubrication,[2] and cold-induced shape recovery.[21] Nevertheless, due to its inherent homogeneous network and the presence of thermal-insensitive chemical crosslinks, the heat-induced modulus change of PAA/calcium acetate hydrogel is still limited, especially in comparison with other stimuli-activated mechanoadaptive nanocomposite materials (e.g. more than 2600 times storage modulus change was

[*] J. Wu, S. Sun, Prof. P. Wu
State Key Laboratory for Modification of Chemical Fibers and Polymer Materials, College of Chemistry, Chemical Engineering and Biotechnology & Center for Advanced Low-dimension Materials, Donghua University
Shanghai 201620 (China)
E-mail: shengtongsun@dhu.edu.cn
wupeiyi@dhu.edu.cn

B. Wu
Jülich Centre for Neutron Science (JCNS) at Heinz Maier-Leibnitz Zentrum (MLZ) Forschungszentrum Jülich
Lichtenbergstr. 1, 85748 Garching (Germany)

Prof. J. Xiong
Innovation Center for Textile Science and Technology, Donghua University
Shanghai 201620 (China)

observed for water-activated cellulose nanofiber-reinforced composites[22]).

In this work, we demonstrate for the first time that physically crosslinked hydrogels relying on entropy-mediated polymer–cluster interactions may serve as an even better candidate for thermal stiffening materials to well reconcile high modulus change amplitude and high mechanical strength at the stiffened state. Our design is inspired by a recent mathematic framework study which implied that the entropy-gain physical adsorption of high molecular weight polymers on the surfaces of nanoparticles would become stronger and less dynamic as temperature increases.[23] To prove this concept, we chose a bioinspired mineral cluster-PAA hydrogel as the representative physical crosslinking system for entropy-mediated polymer-nanoparticle hydrogels, which contains massive mineral clusters (smaller than 3 nm) physically crosslinked by high molecular weight PAA chains ($M_w \approx 100\,000\ g\,mol^{-1}$). By delicately controlling the content of mineral clusters in the hydrogel, a record-high heat-induced storage modulus enhancement of $\approx 13\,000$ times was realized with a super-rapid, dramatic transition from the ultrasoft, reconfigurable state (1.3 kPa) to the stiffened glassy state (17 MPa) (Figure 1a). To demonstrate thermal stiffening applications, we further hybridized the mineral hydrogel and elastic polyacrylamide (PAAm) hydrogel in a bicontinuous structure and produced long fluoroelastomer-coated sheath–core fibers. The hydrogel sheath–core fiber can be further woven into stretchable

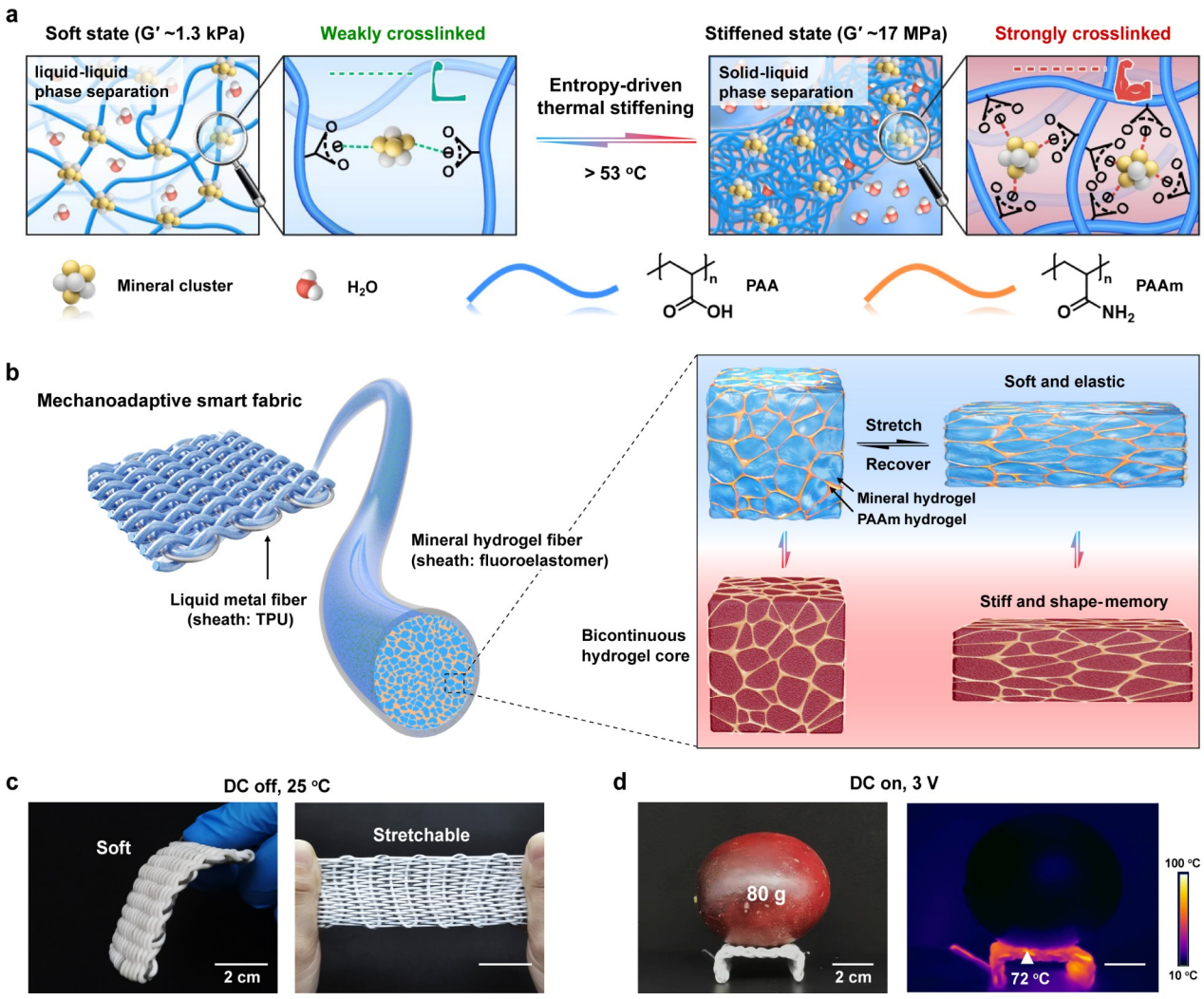

Figure 1. a) Schematic mechanism for dramatic thermal stiffening mineral hydrogels enabled by entropy-mediated polymer–cluster interactions. Upon heat above 53 °C, mineral hydrogel undergoes a sharp transition from the soft reconfigurable state (liquid-liquid phase separation, weakly crosslinked) to the stiffened glassy state (solid–liquid phase separation, strongly crosslinked). b) Schematic design of mineral hydrogel-based mechanoadaptive smart fabric. Hybridizing mineral hydrogel with PAAm hydrogel in the bicontinuous structure results in thermal stiffening elastic hydrogel and corresponding sheath–core fibers. By further co-weaving another liquid metal fiber, a smart fabric with both mechanoadaptive and self-powered sensing properties is finally prepared. c) Photos of soft and stretchable smart fabric at room temperature (DC off). d) Normal and infrared thermal images of a stiffened shape-memorized fabric (7 g) supporting a big fruit (Passiflora edulis Sims, 80 g) when DC voltage (3 V) is on.

fabrics involving another liquid metal fiber (sheath: thermoplastic polyurethane, TPU) as both the joule heater and triboelectric layer for controllable heating and self-powered sensing uses (Figure 1b). The resultant smart fabric inherited the thermal stiffening properties of mineral hydrogel, which was soft and stretchable at room temperature (DC voltage off), yet instantly stiffened in memorized shapes to support a heavy load at elevated temperatures (DC voltage on) (Figure 1c,d, Movie S1). Moreover, such a mechanoadaptive smart fabric may be also used for self-powered force, strain, and temperature sensing while maintaining self-protection functions. It is highlighted that, despite recent emerging applications of smart fabrics in sensing,[24] actuating,[25] thermal regulation,[26] display,[27] and energy storage,[28] we presented the first example of mechanoadaptive fabrics that are not only highly elastic but also actively tune their mechanical properties in response to temperature changes.

Results and Discussion

Entropy-Driven Thermal Stiffening Behavior of Mineral Hydrogel

Mineral hydrogels were facilely prepared by mixing the aqueous solutions of PAA/$CaCl_2$ and Na_2CO_3 which yielded a paste-like hydrogel containing large amounts of amorphous calcium carbonate (ACC) mineral clusters. We have previously demonstrated that the resulting mineral hydrogel is in a liquid-like coacervate state from liquid–liquid phase separation, resembling the polymer-induced liquid precursor in biomineralization.[29,30] The physical crosslinking is formed mainly by the ionic complexation between the exposed Ca^{2+} of ACC clusters and the carboxylate groups of PAA chains, rendering mineral hydrogel highly reconfigurable to be molded into arbitrary shapes. Even dried, the original state can easily recover by swelling in water again. Note that, the used mineral clusters have a comparable diameter with the mesh size of polymer network, which is important to control the amount of adsorbed polymer strands for a proper physical crosslinking strength; larger particles may anchor too many polymer chains resulting in slower chain dynamics and even loss of reconfigurable properties.[23,31]

We carefully adjusted the mixing ratio of two aqueous solutions to optimize the thermal stiffening behavior of mineral hydrogels. When the feed volume ratio of PAA/$CaCl_2$ to Na_2CO_3 equaled to 2:1, a maximum stiffening enhancement of ≈13000 times was observed, reflected by the drastic increase of shear storage modulus (G′) from 1.3 kPa at 27 °C to 17 MPa at 80 °C (Figure 2a). Such a heat-induced significant modulus enhancement was ultra-rapid in 1 s and completely reversible, although the recovering process was relatively slow (ca. 1 h). The slightly higher loss modulus (G″) than G′ at room temperature proves the liquid-like coacervate state of mineral hydrogel, which easily deforms upon compression. However, heating to temperatures above 65 °C forces the hydrogel into a glassy state with much higher G′ than G″. At this state, a 6.8 g of stiffened mineral hydrogel could easily support 1 kg of load without apparent deformation. Even if the hydrogel partially dehydrated at high temperatures, immersing it in cold water for re-swelling can recover all the thermal stiffening properties (Figure S1).

Increasing the added content of Na_2CO_3 would produce more ACC clusters, leading to a relatively higher initial modulus, while less Na_2CO_3 made the glassy modulus plateau even disappear (Figure S2). If Na_2CO_3 was replaced by NaOH, a viscous Ca-PAA hydrogel containing no ACC clusters was obtained with the maximum G′ enhancement being greatly reduced to 3400 times (Figure S3). These control experiments strongly reveal the important role of polymer–cluster interactions in the dramatic thermal stiffening behavior of mineral hydrogels, which also make our design largely differ from the previously reported thermal stiffening hydrogels with a relatively homogeneous network.[12,15–18,20]

To highlight the unprecedented thermal stiffening effect of ACC-PAA mineral hydrogel, we compared the storage modulus changing ranges and stiffening enhancements among a few previously reported thermal stiffening materials. Note that, Young′s modulus determined from tensile or compressive tests was not chosen as the evaluating parameter in this work due to large calculation errors, while storage modulus determined from rheological or dynamic mechanical analysis (DMA) tests is much more reliable for comparison. As shown in Figure 2b and Table S1, the 13000 times storage modulus enhancement of mineral hydrogel is obviously a record-high value for thermal stiffening materials, which covers a wide modulus regime from ultrasoft (e.g. brain, 1–3 kPa) to supertough human tissues (e.g. cartilage, ≈6 MPa).[32] In contrary, other reported thermal stiffening materials suffer from either limited modulus changing ranges or low moduli at the stiffened state.

To determine the exact stiffening temperature ($T_{stiffening}$) of ACC-PAA mineral hydrogel, we performed differential scanning calorimetry (DSC) measurements to track the heating process. Distinct from the phase transitions of LCST-type polymers, no apparent enthalpic peak was observed in the DSC heating curve of mineral hydrogel, but a glass transition-like endothermic shift centered at ≈53 °C indicates the occurrence of entropy-mediated stiffening behavior (Figure S4). Such a transition is closely related to the reduced solubility of Ca^{2+}:COO^- complex at this temperature, which was also observed in calcium acetate/propionate solutions and Ca^{2+}-crosslinked PAA systems.[20,33,34] Increasing heating rates would slightly increase the stiffening temperature, suggesting the presence of two or more competitive events with different relaxation times. The entropy-mediated physical crosslinking nature of mineral hydrogel was further confirmed by the frequency-dependent normalized G′ at different temperatures. As shown in Figure 2c, increased temperatures slowed the dynamics of ACC cluster-PAA network relaxation and resulted in the leftward shifts of G'/G_0 (G_0 was taken at f = 40 Hz) signifying a longer terminal relaxation time.[23] The entropy-driven formation of mineral hydrogel is mainly due to the significant entropy gain as semi-ordered surrounding

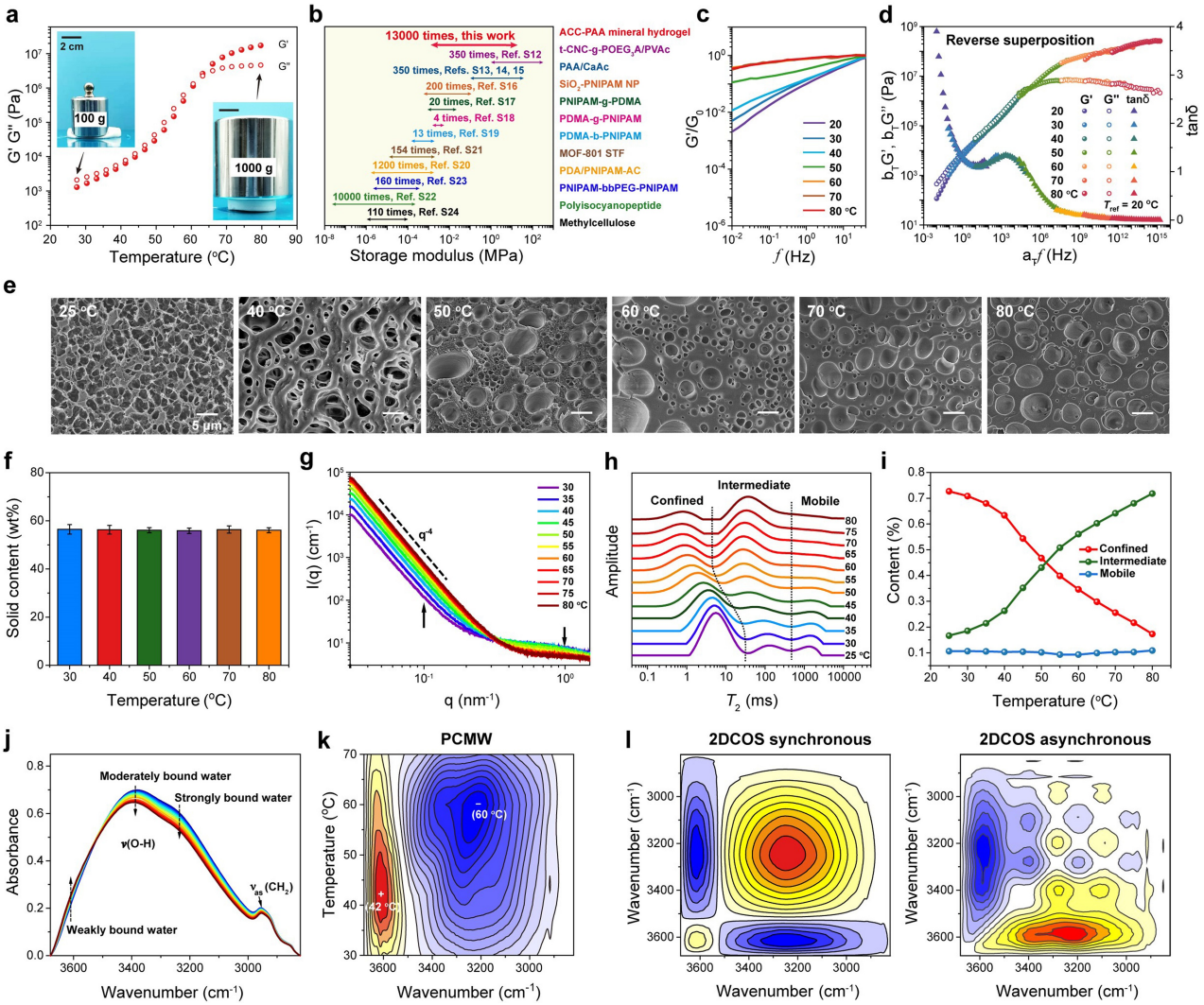

Figure 2. a) Temperature-dependent rheology of ACC-PAA mineral hydrogel. The insets show the hydrogel's deformability at low and high temperatures, respectively. b) Comparison of storage modulus changing range and enhancement factor of the present ACC-PAA mineral hydrogel with other reported thermal stiffening materials. c) Frequency-dependent G'/G_0 curves with increasing temperatures. d) Reverse time–temperature superposition rheological curves at the reference temperature of 20 °C. e) SEM images of lyophilized mineral hydrogels. The samples were prepared by quenching pre-heated hydrogels to different temperatures in liquid nitrogen followed by freeze-drying. f) Temperature-dependent solid content changes of mineral hydrogel. g) Temperature-dependent SAXS curves. h,i) Temperature-dependent low-field ^{1}H NMR curves and corresponding content changes of three kinds of water molecules. j) Variable-temperature FTIR spectra in the regions of ν(O–H) and ν(C–H) from 30 to 70 °C (interval: 2 °C). k, l) PCMW spectrum and 2DCOS synchronous and asynchronous spectra generated from (j). In the 2D spectra, warm colors (red and yellow) represent positive spectral intensities, while cold colors (blue) represent negative ones.

water molecules are dispelled upon the binding of PAA chains on mineral clusters.

In contrast to common physical crosslinking systems with weakened crosslinking at elevated temperatures, thermal stiffening ACC-PAA mineral hydrogel shows an unusual reverse time-temperature superposition rheological behavior with longer timescales at lower temperatures (Figure 2d). The master curve of mineral hydrogel at the reference temperature of 20 °C can be separated into three regimes. In the low-frequency region (< 10 Hz), viscous flow occurs ($G' < G''$), corresponding to the reconfigurable network with weak ionic complexation. In the middle range of 10–10^5 Hz, G' and G'' almost overlap, indicating very high dissipative relaxation caused by the dynamic association of network strands on ACC clusters. The superimposed curves in this regime were recorded between 30 and 50 °C with a maximum loss factor ($\tan\delta = G''/G'$), indicating that entropic sticky Rouse modes based on the motions of Gaussian submolecules are dominating before stiffening.[35] The third regime above 10^5 Hz is assigned to the glassy regime where polymer network is frozen and chain movements are largely restricted. There is no elastic plateau in the master curve, indicating that the network structure of mineral hydrogel is highly dynamic with a relatively small contribution from chain entanglement.[36] $T_{stiffening}$ was calculated to be 52.6 °C from the Boltzmann fitting curve of temperature-dependent

horizonal translation factors (Figure S5), consistent with DSC results.

The physical crosslinking densities were further determined from temperature-dependent compressive moduli,[37] which increased drastically from 1.8 mol m^{-3} at 30 °C to 1.2 × 10^4 mol m^{-3} at 80 °C (Figures S6, S7). Such a remarkable rise of crosslinking density is accompanied by the internal microstructural changes. As shown in the SEM images of lyophilized hydrogels which were prepared by rapidly quenching the pre-heated samples to different temperatures in liquid nitrogen (Figure 2e), the gel was relatively homogeneous with loosely distributed pores at low temperatures, corresponding to liquid-liquid phase separation. However, as temperature increased, large pores gradually appeared and the gel matrix became more densified. An intermediate state with mixed morphologies was observed at 50 °C near the stiffening temperature. Such an observation suggests the occurrence of solid–liquid phase separation with microsyneresis at elevated temperatures, in which gel matrix dehydrated and solidified with the released water trapped in the large pores. The microsyneresis of mineral hydrogel leads to the macroscopic invariance of both volume and mass,[20] as supported by almost equal solid content of 56 wt % from 30 to 80 °C (Figure 2f). In addition, the liquid-liquid to solid–liquid structural transition was also evidenced from the real-time optical microscopic observation of mineral hydrogel in the natural cooling process (Movie S2). At 80 °C, solid–liquid phase separation exhibited a typical granular morphology, which gradually diminished during cooling.

Temperature-dependent small-angle X-ray scattering (SAXS) and very small-angle neutron scattering (VSANS) methods were further used to monitor the microstructural changes in the thermal stiffening process of mineral hydrogel. SAXS mainly reveals the information about structural evolution below 100 nm. As shown in Figures 2g, S8, and S9, as temperature increased, the scattering intensity of mineral hydrogel increased in the low q regime (<0.3 nm^{-1}) but decreased in the high q regime (>0.3 nm^{-1}) both in a sigmoid manner, typical for phase transitions. The calculated correlation length that implies the interchain distance of network decreased from ≈3 Å at 30 °C to ≈0.5 Å above 70 °C, indicating that the hydrogel structure became much denser in the stiffening process. The scattering power law exponents at all temperatures are around −4 in the small q regime indicating the globular dense structure. Complementally, VSANS focuses on the structural evolution in the range of 100 nm−6 μm. As shown in Figure S10, a plateau at small and medium q regimes indicates the formation of globular clusters. With temperature increased, the radius of gyration (R_g) decreased drastically from ≈700 to ≈300 nm, corresponding to the reduction of phase-separated domain size from ≈1.8 to ≈0.8 μm (2.58 times R_g). The calculated phase-separated domain size of 0.8 μm at the stiffened state is well consistent with the optical microscopic observation (Figure S11). Moreover, the scattering power law exponent increased from −3 to −4 in the large q regime, suggesting again that the scatterer became denser. The combined SAXS and VSANS analyses jointly reveal the aggregation and merging of hydrogel network hierarchically upon heat which generated collapsed structures with the sizes of hundreds of nanometers.

Judging from the above analyses, the dehydration of gel matrix at the molecular level seems to be the key to the formation of stiffened network. We therefore employed low-field ^{1}H NMR and 2D correlation IR to clarify the dehydration-related events with increasing temperatures. In low-field ^{1}H NMR, spin-spin relaxation time (T_2) reflects the degree of freedom of hydrogen atoms mainly in water, and a longer T_2 means the better fluidity of water molecules.[11] As shown in Figure 2h, three kinds of water with increasing fluidity–confined, intermediate, and mobile water–coexisted in the hydrogel due to phase separation. As temperature rose to $T_{stiffening}$, an accelerated transformation from confined water (bound to gel matrix) to intermediate water (trapped in the large pores) took place (Figure 2i), supporting the above observations of the transition from liquid-liquid to solid–liquid phase separations.

Temperature-variable FTIR spectra of ACC-PAA mineral hydrogel were recorded between 30 and 70 °C to evaluate the respective thermal responsiveness of different groups. As shown in Figure 2j, as temperature rose, the amount of weakly bound (intermediate) water increased in the expense of moderately and strongly bound water (corresponding to the confined/mobile water as observed by low-field NMR). Meanwhile, CH_2 asymmetric stretching vibration of PAA at around 2958 cm^{-1} shifted to lower wavenumbers, indicating that PAA backbone indeed dehydrated in the stiffening process.[38] Perturbation-correlation moving window (PCMW) calculated the transition temperature of intermediate water to be 42 °C and that of confined/mobile water to be 60 °C (Figure 2k), suggesting that intermediate water had a much faster response to heat than confined/mobile water. 2D correlation spectra (2DCOS) were further generated to determine the thermal responsive sequence of different kinds of water molecules. Based on Noda's judging rule,[39] according to the signs of cross-peaks in the synchronous and asynchronous spectra (Figure 2l, Table S2), the sequential order with increasing temperature was deduced to be as follows: ν(OH) (weakly bound water, 3587 cm^{-1})→ν_s(CH_2) (2848 cm^{-1})→ν(CH) (2914 cm^{-1})→ν-(OH) (strongly bound water, 3282/3199/3109 cm^{-1})→ν_{as}-(CH_2) (2958 cm^{-1})→ν(OH) (moderately bound water, 3396 cm^{-1}) (→means prior to or earlier than). This sequence is in accordance with PCMW results, and further supports that the thermal stiffening behavior of mineral hydrogel is driven by the release of intermediate water molecules. The following response from the C–H stretching vibrations of PAA chains suggests the concurrence of water release (microsyneresis) and polymer dehydration. Moreover, no apparent peak shift of ν(COO^-) at 1552 cm^{-1} was observed (Figure S12), revealing that the Ca^{2+}:COO^- crosslinking strength did not change in the stiffening process. It is thus presumed that the observed increasing crosslinking densities at high temperatures should mainly arise from increasing crosslinking sites for entropy gain, i.e. more physical adsorptions of PAA chains on mineral clusters are formed, as depicted in Figure 1a.

Altogether, the above observations and analyses demonstrate that ACC-PAA mineral hydrogel indeed represents the new conceptual entropy-mediated polymer-nanoparticle physical crosslinking network with a dramatic thermal stiffening behavior. As temperature rises, the sharp transition from liquid-liquid to solid–liquid phase separations occurs, resulting in a dehydrated and densified gel network with significantly increased crosslinking density. At the molecular level, the stiffening process is driven by the release of intermediate water molecules along with PAA dehydration, which jointly contribute to the enhanced polymer-nanoparticle interactions at elevated temperatures. It is thus understandable that, upon cooling, the reverse diffusion of the trapped water from large pores to densified phase cannot readily occur, resulting in a relatively slow recovering process. However, the grain boundaries among phase separated domains may serve as continuous channels to promote water diffusion.

Mineral Hydrogel-Based Mechanoadaptive Smart Fiber

Benefiting from the dramatic thermal stiffening response of mineral hydrogel, mineral hydrogel-based mechanoadaptive devices and wearables may be fabricated. In our work, we focused on utilizing mineral hydrogel to fabricate mechanoadaptive and stretchable smart fibers and fabrics. It is reported that physically crosslinked hydrogels with a reconfigurable and regenerated network show great potential to be processed into any shapes while maintaining original functions.[29,40] We therefore in situ polymerized mineral hydrogel/PAAm precursor paste in a fluoroelastomer tube to form a sheath–core fiber which combined the thermal stiffening ability, elasticity, and water proofness. It is noted that, without introducing PAAm hydrogel phase for improving fiber's elasticity and creating sheath–core interfacial covalent adhesion, the stable and reversible conformal deformation of mineral hydrogel with elastomer sheath will be difficult.

Fluoroelastomer tubes were prepared by a wet-spinning process using poly(vinylidene fluoride-co-hexafluoropropylene-co-tetrafluoroethylene) (PVDF-HFP-TFE) terpolymer/ethyl acetate solution as the sheath flow and ethanol as both the core flow and coagulation bath. Benzophenone was also added to the sheath flow to guarantee the tight interfacial bonding in the post-polymerization process.[41] Mineral hydrogel/PAAm precursor paste was prepared by mixing the ground powder of freeze-dried ACC-PAA and PAAm hydrogel prepolymer solution involving AAm monomer, photoinitiator, crosslinker, as well as 1 wt% P(AAm-co-AA) as rheology modifier. During stirring, mineral gel powder swelled to regenerate, and the precursor paste was obtained in 10 h. Notably, an appropriate mineral gel powder size of $\approx$100 μm was tested to be most suitable for the formation of a uniform and injectable paste, while too small ($\approx$50 μm) and too large ($\approx$200 μm) particle sizes both caused the uncontrolled agglomeration of regenerated mineral hydrogel (Figure S13). In addition, the content of ACC-PAA in the paste is also key to the thermal stiffening response of the final hydrogel fiber, as only a bicontinuous structure can enable the inheritance of both the benefits of the two components. As tested by DMA, the optimal solid content of ACC-PAA was found to be 82 wt%; incorporating more or less ACC-PAA both led to reduced or even disappearance of thermal stiffening behavior due to the failed formation of bicontinuous structure (Figures S14, S15). The optimized hydrogel precursor paste exhibited typical shear-thinning behavior suitable for extrusion into the fluoroelastomer tube (Figure S16). Moreover, neither ACC-PAA mineral hydrogel nor the final bicontinuous hydrogel showed any indication of $CaCO_3$ crystallization (Figure S17), suggesting the mixing process retained the amorphous structure of mineral clusters.

With this method, mineral hydrogel sheath–core fiber could be obtained as long as 2 m with a typical core diameter of 900 μm and sheath thickness of 50 μm (Figure 3a, b). The sheath–core fiber is highly stretchable with a maximum elongation of 1400 % and Young's modulus of 1.4 MPa, with mechanical properties between fluoroelastomer tube (sheath) and bicontinuous hydrogel fiber (core) (Figure 3c). Owing to the good elasticity of sheath and core materials, the sheath–core fiber is highly elastic with fast recovery. Reversibly stretching the fiber to 400 % strain produced almost overlapped stress-strain curves after the first cycle (irreversible structural fracture often occurred in the first cycle) (Figure 3d). The good elasticity of the sheath–core fiber was further supported by cyclically stretching the fiber with increasing strains to 1200 %, whose tensile curves coincided well with the single curve to break (Figure S18). Notably, the conformal deformation of fluoroelastomer sheath and hydrogel core benefits from the tight interfacial adhesion between these two layers assisted by the benzophenone-coupling strategy. The interfacial toughness between sheath and core materials calculated by 90° peeling test is as high as 196 $J\,m^{-2}$; without benzophenone treatment, the adhesion is very weak with a low interfacial toughness of 41 $J\,m^{-2}$ (Figure S19). Furthermore, thanks to the protection of water-proof fluoroelastomer, at room temperature, only a slight weight loss of 4.4 wt% was observed for the sheath–core fiber in 10 days, yet more than 50 wt% weight loss took place in only one day for bare hydrogel fiber due to severe dehydration; even stored at elevated temperatures (60 and 80 °C), the dehydration issue was also significantly inhibited (Figure S20).

Several microscopic tools were employed to verify the bicontinuous structure of the hydrogel core. As demonstrated by SEM and corresponding elemental mapping images (Figures 3e, S21), the hydrogel core is composed of interconnected particulate ACC-PAA mineral phase and another PAAm hydrogel phase filling the particle gaps. The continuous structure of PAAm hydrogel phase was supported by the laser scanning confocal microscopic (LSCM) image, in which the dyed PAAm hydrogel clearly exhibited an interconnected 3D network (green) surrounding the mineral hydrogel phase (black) (Figure 3f). Upon stretching, the stressed elastic PAAm hydrogel phase demonstrated a strong interference blue color, while the mineral hydrogel phase was reconfigurable showing weak interference colors,

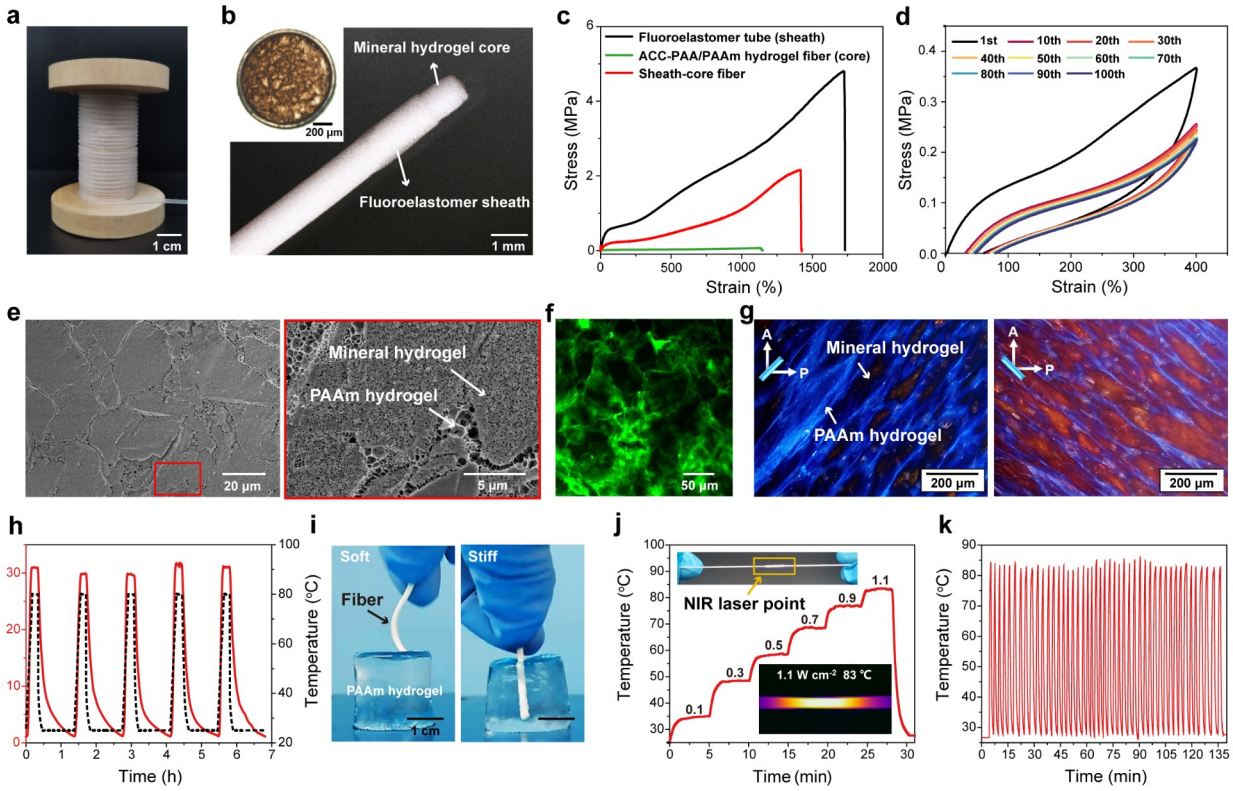

Figure 3. a) Photo of a 2-meter-long mineral hydrogel sheath–core fiber. b) Optical microscopic images of the outer surface and cross-section of sheath–core fiber. c) Tensile curves of sheath–core fiber, fluoroelastomer tube (sheath), and ACC-PAA/PAAm hydrogel fiber (core). d) Cyclic stress-strain curves of sheath–core fiber at the fixed strain of 400% for 100 cycles (stretching rate: 200 mm min^{-1}; waiting time: 3 min). e) SEM images of lyophilized bicontinuous hydrogel fiber core. The right image is the enlarged view of the marked rectangular area. f) LSCM image of the bicontinuous hydrogel with PAAm hydrogel phase dyed by using 8-anilinonaphthalene-1-sulfonic acid. g) POM images of a bicontinuous hydrogel thin film stretched to 100% strain at the azimuth angles of 45° and −45°, respectively. h) DMA cyclic tests demonstrate the reversible thermal stiffening response of sheath–core fiber. i) Photos of the sheath–core fiber being inserted into a PAAm hydrogel at the soft and stiff states. j) Stepwise heating curve of Au NR-incorporated sheath–core fiber with increasing NIR power densities from 0 to 1.1 W cm^{-2}. The insets show the infrared thermal image of the fiber irradiated at the power density of 1.1 W cm^{-2} and a stretched fiber with site-specific stiffening. k) Photothermal stability test by switching the power density of NIR laser between 0 and 1.1 W cm^{-2} for 50 cycles.

as revealed by the polarized optical microscopic (POM) images at different azimuth angles (Figure 3g).

The bicontinuous combination of mineral and PAAm hydrogels enables the final sheath–core fiber both elastic and mechanoadaptive. We measured the storage modulus changes of the fiber with DMA by switching temperature between 25 and 80 °C. As shown in Figure 3h, the fiber instantly stiffened with the storage modulus rising from 1.05 MPa at 25 °C to 32 MPa at 80 °C, corresponding to ca. 30 times modulus enhancement. Such an adaptive stiffening behavior was fully reversible in many heating-cooling cycles. For demonstration, we tried to insert one sheath–core fiber into a soft cylindrical PAAm hydrogel (Figure 3i, Movie S3). At room temperature, the fiber was ultrasoft and unable to induce the deformation of PAAm hydrogel. However, immersing into hot water produced a stiffened fiber which could be easily inserted into the PAAm hydrogel. The comparison of the load-bearing abilities of soft and stiff fibers at different temperatures also confirmed the mechanical adaptability of the resulting sheath–core fiber (Figure S22).

Moreover, since the mineral hydrogel phase in the sheath–core fiber is reconfigurable, shape memory can be easily realized by fixing the fiber in different shapes or even stretched states followed by heating (Figures 1b, S23). Embedding photothermal gold nanorods (Au NRs, λ_{max} = 845 nm; Figures S24, S25) into the mineral hydrogel phase could also impart remote and site-specific stiffening ability to the sheath–core fiber. Increasing the power densities of NIR laser (808 nm) significantly increased the temperature of the fiber, which immediately stiffened at the irradiated point (Figures 3j, S26, Movie S4). The NIR-induced heating and stiffening could be repeated in many times without obvious performance attenuation (Figures 3k, S27).

Mechanoadaptive Smart Fabric

The long mineral hydrogel sheath–core fibers can be further woven into mechanoadaptive braids and fabrics. For example, the fiber may be easily woven into a bowknot or multi-strand ropes (Figure 4a). For mechanoadaptive smart fab-

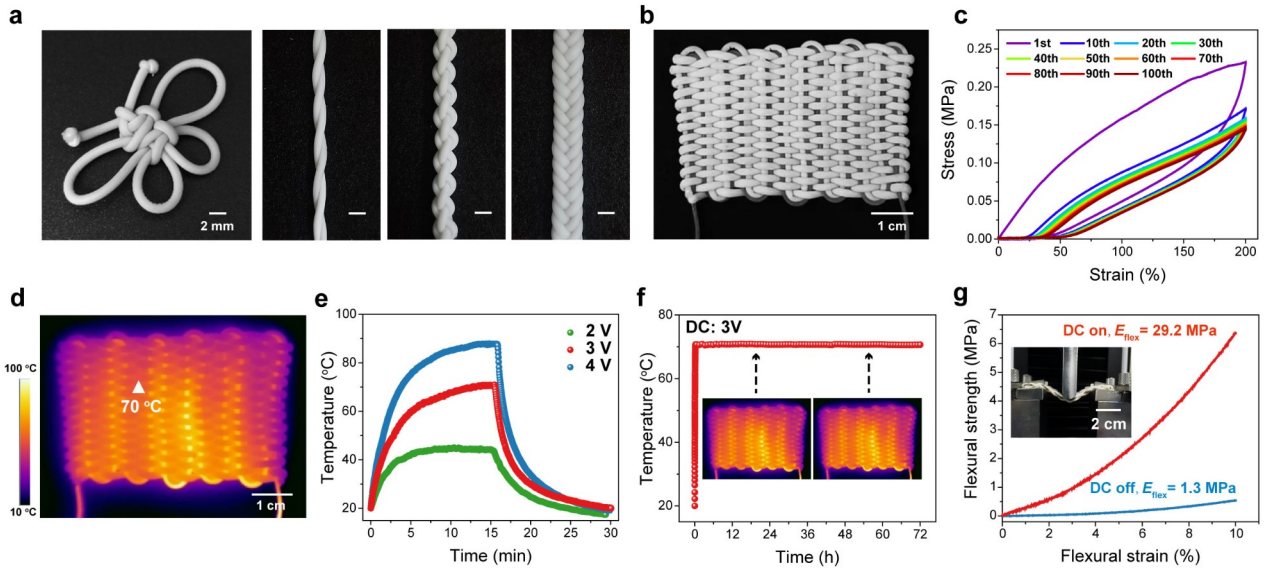

Figure 4. a) Mineral hydrogel sheath–core fibers can be woven into a bowknot and multi-strand ropes using one, two, four, and five fibers, respectively. b) Photo of mineral hydrogel-based smart fabric (5 cm × 4 cm). c) Cyclic tensile curves of the fabric at a fixed strain of 200% for 100 cycles (stretching rate: 200 mm/min; waiting time: 3 min). d) Infrared thermal image of the fabric at the DC voltage of 3 V. e) Electrical heating performance of the fabric at different applied voltages. f) Electrothermal stability at the fixed voltage of 3 V. g) Flexural stress–strain curves of the fabric by switching DC on and off.

rics, the integration of heating source is a more direct way to program the stiffening properties. Among various heating methods, electrical activation or joule heating is more advantageous due to its easy control and natural compatibility with electrical sensing and communication omnipresent in smart electronic devices and robots.[42,43] Therefore, as illustrated in Figure 1b, we employed another elastic liquid metal sheath–core fiber as the joule heater to co-weave with mineral hydrogel sheath–core fiber. The liquid metal sheath–core fiber was prepared by directly filling EGaIn (melting point ≈16 °C) into a wet-spun TPU tube (outer diameter: 0.8 mm; inner diameter: 0.5 mm). It is noted that the tube size is key to joule heating performance: large-size tubes do not allow for effective heating due to the rather low resistance of liquid metal, while too narrow tubes are difficult to uniformly inject the high-surface-tension liquid metal.[44,45]

The woven fabric with interlaced liquid metal and mineral hydrogel sheath–core fibers is soft and highly elastic, which can sustain repeated stretching to 200% strain with almost coincidental curves (Figure 4b,c). At an applied DC voltage of 3 V, the fabric could quickly reach a maximum surface temperature of ≈70 °C which was enough to stiffen mineral hydrogel fibers (Figure 4d, Movie S1). Varying the applied voltage was able to adjust the heated temperatures of the fabric (Figure 4e). If the applied voltage was maintained at 3 V, the surface temperature of the fabric remained stable for more than 72 h, demonstrating the durable heating performance of liquid metal fiber (Figure 4f). Moreover, the thermal stiffening property of mineral hydrogel fiber imparted good mechanical adaptability to the resulting fabric, which stiffened with the flexural modulus increasing from 1.3 MPa at the natural soft state to 29.2 MPa when DC voltage was on, as evaluated by three-point bending measurements (Figure 4g).

Furthermore, the respective electronic and ionic conductivities of liquid metal and mineral hydrogel sheath–core fibers as well as the different electronegativities between TPU and fluoroelastomer bring excellent triboelectric-based self-powered sensing properties to the resulting fabric (schematic working principle in Figure S28).[44] The fabric was shown to output repeatable and reliable voltage signals in response to various stimuli such as pressing frequency and force, stretching, and temperature changes (Figures S29–S32, Movie S5). In practical scenarios like grasping, football catching, and respiration, the fabric was shown to also work very well (Figures S33–S36), demonstrating its great potential in smart sensing applications.

Conclusion

Herein we have reported a new kind of dramatic thermal stiffening mineral hydrogel enabled by entropy-mediated polymer–cluster interactions, which shows an unprecedented storage modulus enhancement of 13000 times, surpassing all the reported thermal stiffening materials. Our detailed analyses elucidated the thermal stiffening nature of mineral hydrogel to be the heat-induced transition from liquid-liquid to solid–liquid phase separations, and at the molecular level, to be entropically driven by the release of intermediate water molecules along with enhanced polymer–cluster interactions. We further demonstrated that the mineral hydrogel can be applied for fabricating smart fibers and

fabrics. Both the mineral hydrogel-incorporated sheath–core fibers and woven fabrics exhibited the dramatic thermal stiffening response, and thus may be potentially used for load-bearing, anti-impact, shape-memory, and self-powered sensing applications. We envision that the strategy of entropy-mediated polymer–cluster interactions shall be easily extended to design other thermal stiffening hydrogels, and for applications, the present mechanoadaptive hydrogels, fibers, and fabrics may shed light on developing more advanced soft robots and wearables.

Acknowledgements

The authors gratefully acknowledge the financial support from the National Science Foundation of China (NSFC) (Nos. 21991123, 51873035, and 51733003) and Qimingxing Plan (No. 19QA1400200). The authors also thank the staff from BL16B beamline at Shanghai Synchrotron Radiation Facility (SSRF) for assistance during data collection.

Conflict of Interest

The authors declare no conflict of interest.

Data Availability Statement

The data that support the findings of this study are available from the corresponding author upon reasonable request.

Keywords: Adaptive Materials · Hydrogels · Sensing · Smart Fabrics · Thermal Stiffening

[1] X. Lin, X. Wang, L. Zeng, Z. Wu, H. Guo, D. Hourdet, *Chem. Mater.* **2021**, *33*, 7633–7656.
[2] Y. Zhang, W. Zhao, S. Ma, H. Liu, X. Wang, X. Zhao, B. Yu, M. Cai, F. Zhou, *Nat. Commun.* **2022**, *13*, 377.
[3] D. Zhao, B. Pang, Y. Zhu, W. Cheng, K. Cao, D. Ye, C. Si, G. Xu, C. Chen, H. Yu, *Adv. Mater.* **2022**, *34*, 2107857.
[4] E. Cudjoe, S. Khani, A. E. Way, M. J. A. Hore, J. Maia, S. J. Rowan, *ACS Cent. Sci.* **2017**, *3*, 886–894.
[5] Y. Wang, L. Li, D. Hofmann, J. E. Andrade, C. Daraio, *Nature* **2021**, *596*, 238–243.
[6] Z. Wang, J. Wang, J. Ayarza, T. Steeves, Z. Hu, S. Manna, A. P. Esser-Kahn, *Nat. Mater.* **2021**, *20*, 869–874.
[7] T. Matsuda, R. Kawakami, R. Namba, T. Nakajima, J. Gong, *Science* **2019**, *363*, 504–508.
[8] D. Zhang, E. Dashtimoghadam, F. Fahimipour, X. Hu, Q. Li, E. A. Bersenev, D. A. Ivanov, M. Vatankhah-Varnoosfaderani, S. S. Sheiko, *Adv. Mater.* **2020**, *32*, 2005314.
[9] B. Liu, Z. Xu, H. Gao, C. Fan, G. Ma, D. Zhang, M. Xiao, B. Zhang, Y. Yang, C. Cui, T. Wu, X. Feng, W. Liu, *Adv. Funct. Mater.* **2020**, *30*, 1910197.
[10] S. Zhuo, Z. Zhao, Z. Xie, Y. Hao, Y. Xu, T. Zhao, H. Li, E. M. Knubben, L. Wen, L. Jiang, M. Liu, *Sci. Adv.* **2020**, *6*, eaax1464.
[11] K. Gong, L. Hou, P. Wu, *Adv. Mater.* **2022**, *34*, 2201065.
[12] P. H. J. Kouwer, M. Koepf, V. A. A. L. Sage, M. Jaspers, A. M. V. Buul, Z. H. Eksteen-Akeroyd, T. Woltinge, E. Schwartz, H. J. Kitto, R. Hoogenboom, S. J. Picken, R. J. M. Nolte, E. Mendes, A. E. Rowan, *Nature* **2013**, *493*, 651.
[13] M. Fernández-Castaño Romera, R. Göstl, H. Shaikh, G. T. Huurne, J. Schill, I. K. Voets, C. Storm, R. P. Sijbesma, *J. Am. Chem. Soc.* **2019**, *141*, 1989–1997.
[14] F. Visentin, S. P. M. Babu, F. Meder, B. Mazzolai, *Adv. Funct. Mater.* **2021**, *31*, 2101121.
[15] H. Guo, N. Sanson, D. Hourdet, A. Marcellan, *Adv. Mater.* **2016**, *28*, 5857–5864.
[16] Y. Hu, L. Barbier, Z. Li, X. Ji, H. L. Blay, D. Hourdet, N. Sanson, J. W. Y. Lam, A. Marcellan, B. Tang, *Adv. Mater.* **2021**, *33*, 2101500.
[17] M. Morimura, S. Ida, M. Oyama, H. Takeshita, S. Kanaoka, *Macromolecules* **2021**, *54*, 1732–1741.
[18] F. Vashahi, M. R. Martinez, E. Dashtimoghadam, F. Fahimipour, A. N. Keith, E. A. Bersenev, D. A. Ivanov, E. B. Zhulina, P. Popryadukhin, K. Matyjaszewski, M. Vatankhah-Varnosfaderani, S. S. Sheiko, *Sci. Adv.* **2022**, *8*, eabm2469.
[19] M. Liu, X. Wan, M. Yang, Z. Wang, H. Bao, B. Dai, H. Liu, S. Wang, *Angew. Chem. Int. Ed.* **2022**, *61*, 202114602; *Angew. Chem.* **2022**, *134*, 202114602.
[20] T. Nonoyama, Y. W. Lee, K. Ota, K. Fujioka, W. Hong, J. Gong, *Adv. Mater.* **2020**, *32*, 1905878.
[21] L. Hua, C. Zhao, X. Guan, J. Lu, J. Zhang, *Sci. China Mater.* **2022**, https://doi.org/10.1007/s40843-021-1971-9.
[22] J. R. Capadona, K. Shanmuganathan, D. J. Tyler, S. J. Rowan, C. Weder, *Science* **2008**, *319*, 1370–1374.
[23] A. C. Yu, H. Lian, X. Kong, H. L. Hernandez, J. Qin, E. A. Appel, *Nat. Commun.* **2021**, *12*, 746.
[24] K. Dong, X. Peng, R. Cheng, C. Ning, Y. Jiang, Y. Zhang, Z. Wang, *Adv. Mater.* **2022**, *34*, 2109355.
[25] T. Jia, Y. Wang, Y. Dou, Y. Li, M. J. D. Andrade, R. Wang, S. Fang, J. Li, Z. Yu, R. Qiao, Z. Liu, Y. Cheng, Y. Su, M. Minary-Jolandan, R. H. Baughman, D. Qian, Z. Liu, *Adv. Funct. Mater.* **2019**, *29*, 1808241.
[26] S. Zeng, S. Pian, M. Su, Z. Wang, M. Wu, X. Liu, M. Chen, Y. Xiang, J. Wu, M. Zhang, Q. Cen, Y. Tang, X. Zhou, Z. Huang, R. Wang, A. Tunuhe, X. Sun, Z. Xia, M. Tian, M. Chen, X. Ma, L. Yang, J. Zhou, H. Zhou, Q. Yang, X. Li, Y. Ma, G. Tao, *Science* **2021**, *373*, 692–696.
[27] X. Shi, Y. Zuo, P. Zhai, J. Shen, Y. Yang, Z. Gao, M. Liao, J. Wu, J. Wang, X. Xu, Q. Tong, B. Zhang, B. Wang, X. Sun, L. Zhang, Q. Pei, D. Jin, P. Chen, H. Peng, *Nature* **2021**, *591*, 240–245.
[28] J. He, C. Lu, H. Jiang, F. Han, X. Shi, J. Wu, L. Wang, T. Chen, J. Wang, Y. Zhang, H. Yang, G. Zhang, X. Sun, B. Wang, P. Chen, Y. Wang, Y. Xia, H. Peng, *Nature* **2021**, *597*, 57–63.
[29] S. Sun, L. Mao, Z. Lei, S. Yu, H. Cölfen, *Angew. Chem. Int. Ed.* **2016**, *55*, 11765–11769; *Angew. Chem.* **2016**, *128*, 11939–11943.
[30] Y. Xu, K. C. H. Tijssen, P. H. H. Bomans, A. Akiva, H. Friedrich, A. P. M. Kentgens, N. A. J. M. Sommerdijk, *Nat. Commun.* **2018**, *9*, 2582.
[31] S. Rose, A. Prevoteau, P. Elziere, D. Hourdet, A. Marcellan, L. Leibler, *Nature* **2014**, *505*, 382.
[32] C. F. Guimarães, L. Gasperini, A. P. Marques, R. L. Reis, *Nat. Rev. Mater.* **2020**, *5*, 351–370.
[33] J. S. Lumsden, *J. Chem. Soc. Trans.* **1902**, *81*, 350–362.
[34] Y. Wu, W. W. J. Zhang, M. Sang, Y. Xu, J. Zhou, S. Wang, Y. Cai, S. Xuan, X. Gong, *Chem. Eng. J.* **2022**, *428*, 131793.
[35] M. Golkaram, K. Loos, *Macromolecules* **2019**, *52*, 9427–9444.
[36] Z. Zhang, L. Cheng, J. Zhao, H. Zhang, X. Zhao, Y. Liu, R. Bai, H. Pan, W. Yu, X. Yan, *J. Am. Chem. Soc.* **2021**, *143*, 902–911.
[37] C. Norioka, Y. Inamoto, C. Hajime, A. Kawamura, T. Miyata, *NPG Asia Mater.* **2021**, *13*, 34.

[38] Z. Ye, S. Sun, P. Wu, *ACS Macro Lett.* **2020**, *9*, 974–979.
[39] W. Zhang, B. Wu, S. Sun, P. Wu, *Nat. Commun.* **2021**, *12*, 4082.
[40] X. Peng, X. Xia, X. Xu, X. Yang, B. Yang, P. Zhao, W. Yuan, P. W. Y. Chiu, L. Bian, *Sci. Adv.* **2021**, *7*, eabe8739.
[41] X. Wen, S. Sun, P. Wu, *Mater. Horiz.* **2020**, *7*, 2150–2157.
[42] D. J. Levine, K. T. Turner, J. H. Pikul, *Adv. Mater.* **2021**, *33*, 2007952.
[43] J. Wang, S. Sun, P. Wu, *SusMat* **2021**, *1*, 545–557.
[44] L. Zheng, M. Zhu, B. Wu, Z. Li, S. Sun, P. Wu, *Sci. Adv.* **2021**, *7*, eabg4041.
[45] Y. Jin, Y. Lin, A. Kiani, I. D. Joshipura, M. Ge, M. D. Dickey, *Nat. Commun.* **2019**, *10*, 4187.